Electrical Power and Energy Systems 152 (2023) 109261

Contents lists available at ScienceDirect

International Journal of Electrical Power and Energy Systems

journal homepage: www.elsevier.com/locate/ijepes

Polarity of current area based active injection protection scheme for hybrid MMC-HVDC grids

Keao Chen [a], Qiteng Hong [b], Meng Li [a,*], Jinghan He [a], Yong Tang [c], Campbell D. Booth [b]

[a] the School of Electrical Engineering, Beijing Jiaotong University, Beijing 100044, China
[b] Department of Electronic and Electrical Engineering, University of Strathclyde, G1 1XW Glasgow, UK
[c] the China Electrical Power Research Institute, Beijing 100192, China

ARTICLE INFO

Keywords:
Hybrid MMC
TW analysis
Measured terminal current
Active injection protection
Polarity of current area

ABSTRACT

With the massive increase of power electronic devices to facilitate renewable integration, the system's fault characteristics will be dramatically changed due to the different control strategies adopted by converters. As a result, the dependability and security of the traditional protection can be severely compromised. Considering the high controllability of power electronic converters, this paper presents an active injection protection scheme to effectively identify the fault. By analyzing the traveling wave (TW) refraction and reflection characteristics under different fault conditions, the variation of the measured terminal current caused by the TW is revealed. Then, a rectangular wave is injected by the hybrid modular multilevel converters (MMC) for a short time after the fault ride-through process. By introducing the concept of the polarity of the current area, the proposed protection scheme only needs to measure the terminal current without any complex signal extracting and processing algorithm to identify the internal and external faults. The feasibility and effectiveness of the proposed protection scheme are verified by realistic case studies with simulation conducted in the PSCAD platform.

1. Introduction

With the rapid development of power electronic equipment, the voltage source converter (VSC) based high-voltage direct current (HVDC) has been a promising technology to enable multi-terminal HVDC grids [1]. VSC-HVDC systems have many outstanding advantages including capability in large-scale renewable energy integration, high-capacity power transmission, decoupled control of active and reactive power, and convenient systems interconnection [2–3]. Furthermore, in contrast to the traditional HVDC technology, VSC-HVDC systems are subject to the risk of commutation failure due to the fundamentally different working mechanism [4]. However, the DC grid is a system with low impedance. After a DC fault, the fault current can rise rapidly, presenting a significant threat to the fragile power electronic equipment.

In order to avoid the damage to power electronic equipment, various methods have been proposed to limit the fault currents. A common method is to install the large current limiting reactors (CLR) [5–6]. However, the large CLR increases the investment and can negatively influence the stability of the system. There are also some current limiting methods based on the high controllability of converters being proposed. As highlighted in [7], the main contribution of the fault current is from the discharge of sub-module (SM) capacitors. Therefore, the current limiting strategy based on the half-bridge modular multilevel converter (HB-MMC) is proposed [8–9]. The number of inserted SMs is reduced temporarily following the detection of a fault. For the full-bridge MMC (FB-MMC) and the hybrid-MMC using both full-bridge sub-modules (FBSM) and half-bridge sub-modules (HBSM), they can realize the fault current limiting and fault ride-through by outputting the negative voltage from the FBSMs [10–11]. Furthermore, the FB-MMC and the hybrid-MMC have reactive power compensation capability during the fault ride-through process and advantages in rapid recovery after the faults [12]. However, these converter control strategies will change the original fault characteristics, and the performance of the traditional protection will be further challenged.

Travelling wave (TW) protection schemes are extensively applied as the primary protection in MMC-HVDC grids [13]. In real-world implementations, TW protection schemes that measure the change of voltage and current at the terminal to identify faults with fast operation speed are typically adopted [14]. However, they are often unable to identify internal faults with high impedance, and they can be sensitive to the impact of measurement noise. The threshold for determining fault or

* Corresponding author.
E-mail addresses: q.hong@strath.ac.uk (Q. Hong), mengl@bjtu.edu.cn (M. Li), tangyong@epri.sgcc.com (Y. Tang), campbell.d.booth@strath.ac.uk (C.D. Booth).

https://doi.org/10.1016/j.ijepes.2023.109261
Received 28 November 2022; Received in revised form 4 April 2023; Accepted 16 May 2023
Available online 23 May 2023

non-fault conditions often relies on simulation, so there are significant limitations. Under the control strategies of converters, the effective time window is shorter, and the protection performance is further affected. Some boundary-condition based protection schemes are proposed in [15–16]. The fault direction can be identified by the different fault characteristics on two sides of CLR. However, under the fault current limiting effect of converters, the size of CLR will decrease, and the reliability and sensitivity of the protection will be affected. A setting-less protection method is proposed to identify the faults with good robustness [17], which measures the voltage in a very short time window, and uses the optimal approximation method to recognize the fault mode. Although the information acquired is not severely affected by the control strategies of the converter, there are high requirements for sampling frequency and calculation capability. In addition, some pilot protection schemes are proposed with high reliability. The studied objective of these schemes is changed from the fault characteristics at one terminal to the state of the transmission line [18–19]. Therefore, the influence of control strategies of the converter can be eliminated theoretically. However, the protection schemes are computationally intensive and have a heavy communication burden.

Therefore, it is necessary to explore new protection schemes to address the various limitations with the existing protection solutions as discussed above. Considering the high controllability of power electronics equipment, the converters can not only have the function of limiting the fault current but also intentionally create the identifiable feature for protection. In the photovoltaic DC integration system, some active injection methods have been proposed to identify the faults [20–21]. The DC/DC converters are modified to be frequency-controllable injection sources for the realization of the protection. An active injection protection scheme is proposed to identify faults with a square signal in the two-terminal HVDC network [22], but the requirement of selectivity in the DC grid needs to be further verified. A correlation algorithm based protection scheme is proposed to realize the fault identification by generating signals in different frequencies [23]. With the integration of control and protection, these protection schemes can identify the faults reliably. However, these schemes often need to inject signals of multiple frequencies into the network and have high requirements on the particular characteristics of the signals. At the same time, some signal processing algorithms are needed to extract the characteristics of the injected signal, presenting a high requirement on computation power.

According to the current research status, the active injection based protection schemes should be further improved. In this paper, an active injection protection scheme is proposed to identify the faults. Based on the hybrid-MMC, the rectangular wave is injected into the grid after the fault ride-through process. Then the faulty zone can be identified by the polarity of the current area (i.e. a quantity defined in the proposed protection algorithm associated with integral of current over time, which will be explained in detail in Section VI). Compared with the current active injection protection scheme, the proposed scheme only uses the measured current at the terminal, and complex signal processing tools are not required.

The rest of the paper is structured as follows. In Section II, the operating principle of the proposed protection is introduced. In Section III, the characteristics of the injected TW from the MMC are analyzed, including the propagation process in the transmission line and the principles of reflection and refraction. In Section IV, the different characteristics of the measured terminal current are discovered. In Section V, the control strategies of the MMC are proposed in different stages. In Section VI, the overall scheme of the proposed protection based on the polarity of current area is constructed. In Section VII, the feasibility of the protection is verified in a three-terminal hybrid MMC-HVDC grid modelled and simulated in PSCAD. Finally, the conclusion is drawn in Section VIII.

Idea of Realizing Active Injection Protection Scheme.

According to the multi-terminal MMC-HVDC grid shown in Fig. 1,

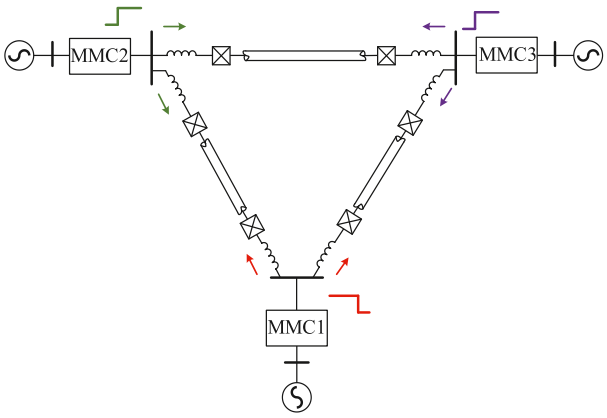

Fig. 1. Schematic diagram of multi-terminal MMC-HVDC grid.

the DC faults will cause the rapid rise of fault currents. Therefore, the hybrid-MMCs with FBSMs limit the fault currents quickly to ride-through the fault. However, the fault currents are with lower amplitude and are different from the original fault characteristics under the HB-MMC based HVDC grid. For enhanced reliability, the MMCs with FBSMs can be controlled in a particular order, i.e. injecting rectangular TWs into the transmission lines to identify the fault after the fault ride-through process.

Characteristics of Injected TW.

A. Propagation characteristics of TW.

The analysis of TW relies on distributed parameters model of the transmission line shown in Fig. 2, where R_u, L_u, G_u, and C_u denote series resistance, series inductance, parallel conductance, and parallel capacitance per unit length, respectively; $u(x, t)$ and $u(x + \Delta t, t)$ are the voltages at both terminals; and $i(x, t)$ and $i(x + \Delta t, t)$ are the currents at both terminals. The energy of transient excitation is exchanged with each other in the distributed inductance and capacitance, gradually diffuses, and propagates in the form of TW. Therefore, when the TW front arrives, the voltage and current in the transmission line will change accordingly.

Based on the circuit, the telegraph equation can be expressed as:

$$\begin{cases} -\dfrac{\partial^2 u(x,t)}{\partial x \partial t} = R_u \dfrac{\partial i(x,t)}{\partial t} + L_u \dfrac{\partial^2 i(x,t)}{\partial t^2} \\ -\dfrac{\partial^2 i(x,t)}{\partial x \partial t} = G_u \dfrac{\partial u(x,t)}{\partial t} + C_u \dfrac{\partial^2 u(x,t)}{\partial t^2} \end{cases} \tag{1}$$

The Laplace transform is used to solve (1) in the complex frequency domain. Then the D' Alembert solutions are [24]:

$$\begin{cases} u(x,t) = V_f(x - vt) + V_b(x + vt) \\ i(x,t) = [V_f(x - vt) - V_b(x + vt)]/z_c \\ \qquad = I_f(x - vt) - I_b(x + vt) \end{cases} \tag{2}$$

where V_f and V_b are the forward and backward voltage TWs, respectively; I_f and I_b are the forward and backward current TWs, respectively; v is the propagation speed; and Z_c is the wave impedance.

Based on (2), the transmission line in the TW analysis can be equivalent to a lumped parameter, whose value is the wave impedance.

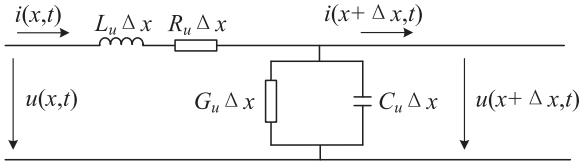

Fig. 2. Distributed parameters model of transmission line.

Therefore, the characteristics of TW reflection and refraction can be analyzed by the Peterson principle.

In addition, the intercoupling effect between the positive and negative poles should be eliminated. The phase-to-mode conversion is:

$$\begin{cases} \begin{bmatrix} u_1 \\ u_0 \end{bmatrix} = \frac{1}{\sqrt{2}} \begin{bmatrix} 1 & 1 \\ 1 & -1 \end{bmatrix} \begin{bmatrix} u_P \\ u_N \end{bmatrix} \\ \begin{bmatrix} i_1 \\ i_0 \end{bmatrix} = \frac{1}{\sqrt{2}} \begin{bmatrix} 1 & 1 \\ 1 & -1 \end{bmatrix} \begin{bmatrix} u_P \\ u_N \end{bmatrix} \end{cases} \tag{3}$$

where u_1 and u_0 are the line-mode and earth-mode voltages, respectively; i_1 and i_0 are the line-mode and earth-mode currents, respectively; u_P and u_N are the positive and negative mode voltages, respectively; and i_P and i_N are the positive and negative mode voltages, respectively. The earth-mode components are affected by the distributed parameters and distort severely. Therefore, this paper uses the line-mode components.

B. Principle of refraction and reflection.

After the fault ride-through process, the selected MMC will inject a rectangular wave into the transmission line, and the schematic diagram of the TW refraction and reflection is presented in Fig. 3. V_i is a rectangular voltage TW injected by the selected MMC. Due to the discontinuity of the impedance, the injected TW will be refracted and reflected at the terminals and the fault point. α_N is the refraction coefficient when the initial rectangular TW propagates through the CLR. β_M and β_N are the reflection coefficient at the terminal M and N, respectively. α_K and β_K are the refraction coefficient and reflection coefficient at the fault point K, respectively.

Firstly, the injected TW V_i will propagate through the CLR, and the diagram is shown in Fig. 4(a). The equivalent circuit can be obtained by the Peterson principle in Fig. 4(b). According to the Peterson equivalent circuit, the refracted TW V_{i1} is:

$$V_{i1} = \frac{2Z_{c1}}{Z_s + Z_{c1} + sL} V_i \tag{4}$$

where Z_{c1} is the line-mode wave impedance of the transmission line; Z_s is the equivalent impedance of the MMC; and L is the inductance of CLR. According to (4), the refraction coefficient can be expressed as:

$$0 < \alpha_N = V_{i1}/V_i < 1 \tag{5}$$

After the propagation through the CLR, the TW will propagate in the transmission line. If there is a fault occurring in the line, the TW propagates to the fault point K firstly, as shown in Fig. 5(a). The Peterson equivalent circuit under the pole-to-pole (PTP) fault is shown in Fig. 5 (b), the refraction coefficient α_K and reflection coefficient β_K can be obtained.

$$0 \le \alpha_K = \frac{R_f}{Z_{c1} + R_f} < 1 \tag{6}$$

$$-1 \le \beta_K = -\frac{Z_{c1}}{Z_{c1} + R_f} < 0 \tag{7}$$

where R_f is the fault resistance.

Similarly, the refraction coefficient α_K and reflection coefficient β_K can be obtained under the pole-to-ground (PTG) fault.

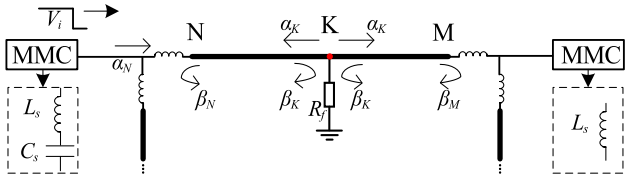

Fig. 3. Schematical diagram of propagation of injected TW.

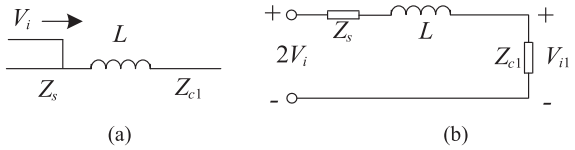

Fig. 4. Injected rectangular wave propagating through CLR.

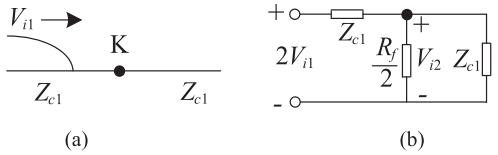

Fig. 5. TW propagation process at fault point.

$$0 \le \alpha_K = \frac{Z_{c0} + 4R_f}{Z_{c1} + Z_{c0} + 4R_f} < 1 \tag{8}$$

$$-1 \le \beta_K = -\frac{Z_{c1}}{Z_{c1} + Z_{c0} + 4R_f} < 0 \tag{9}$$

where Z_{c0} is the earth-mode wave impedance of the transmission line.

Furthermore, the TW will also be reflected at terminals M and N. As shown in Fig. 6(b), the total impedance Z_t at the terminal includes the equivalent impedance of the MMC (Z_s), CLRs (sL), and the wave impedance in the adjacent line (Z_{c1}). The expression of the reflection coefficient is:

$$-1 < \beta_t = \frac{Z_t - Z_{c1}}{Z_t + Z_{c1}} < 1 \tag{10}$$

$$Z_t = sL + [Z_s(sL + Z_{c1})]/(Z_{c1} + Z_s + sL)$$

For the reflection coefficient β_t at the terminal, it is generally within (-1, 1). To determine the value of β_t, a step response of the reflection coefficients is shown in Fig. 7. For the terminal N, Z_s includes the equivalent capacitance (C_S), which shows the negative impedance characteristics. Therefore, the reflection coefficient β_N turns negative rapidly. For terminal M, the equivalent capacitance in the converter is zero. Therefore, the reflection coefficient β_M will decrease with time, but keep positive within the initial 4 ms. In this paper, we only focus on the situation within this initial period. Therefore, it can be considered that the reflection coefficients β_N and β_M are within (-1, 0) and (0, 1) respectively in the subsequent analysis.

2. Characteristics of measured terminal current under different faults

After the fault ride-through process, the DC fault current is limited to zero. Therefore, before the rectangular TW is injected into the transmission line, the measured terminal current i_N in the protection relay N is zero. At the same time, the injected TW refracted and reflected in the transmission line will cause the change of i_N. The changing

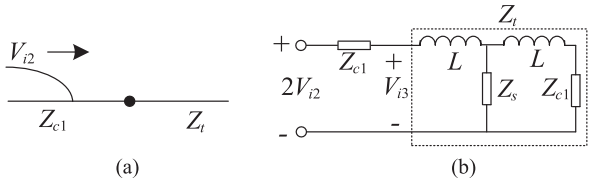

Fig. 6. Diagram of TW propagation process at terminal.

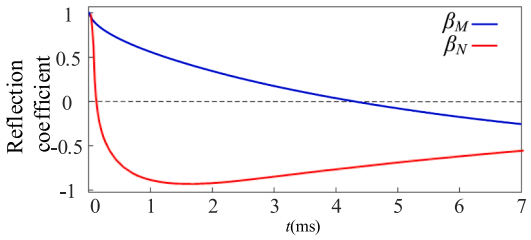

Fig. 7. Response of reflection coefficients to unit step wave.

characteristics of i_N are different in the different fault scenarios. For the analysis of the changing characteristics of i_N, the attenuation of the TW in the transmission line is ignored for simplicity. The lattice diagrams of the injected TW propagation process are shown in Figs. 8-10, which illustrate the scenarios of external fault, metallic internal fault, and the internal fault with resistance, respectively. I_i is the injected current TW by MMC. l is the length of the transmission line. $\times$ is the fault location. v is the propagation speed of the TW. $t_s = 4\ l/v$ is defined as the end time, which includes the four times for the TW to propagate over the entire transmission line.

(1) External faults.

Under an external fault, there is no discontinuity point in the transmission line. As shown in Fig. 8(a), the injected current TW I_i refracts $\alpha_N I_i$ into the transmission line. According to (5), the refraction coefficient α_N is greater than zero. Therefore, the measured current i_N will rise at t_0. During the interval (t_0, t_2), i_N keeps constant, because the reflected TW $\alpha_N\beta_M I_i$ has not arrived at terminal N. According to the analysis in Section III, β_M and β_N are within (0, 1) and (-1, 0), respectively. Therefore, i_N will decrease and increase by $-\alpha_N\beta_M(1-\beta_M)I_i$ and $-\alpha_N\beta_M^2\beta_N(1-\beta_N)I_i$ at t_2 and t_4, respectively. According to the above analysis, the changing characteristics of measured current i_N within (t_0, t_s) are demonstrated in Fig. 8(b). It can be seen that i_N reaches the largest value within (t_0, t_2) and then decreases within (t_2, t_4). The shaded current area s_1 enclosed by the value of current i_N at t_2 and the measured value of current i_N within (t_2, t_s) is negative.

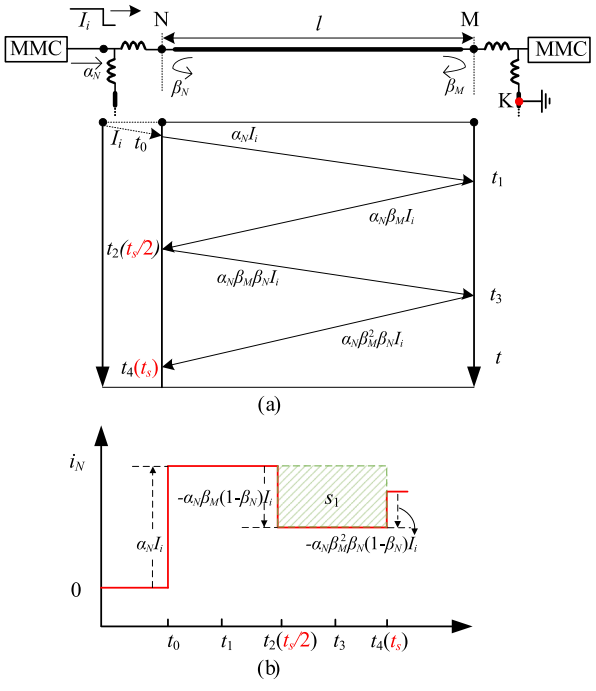

Fig. 8. Lattice diagram of injected TW and characteristics of i_N under external fault.

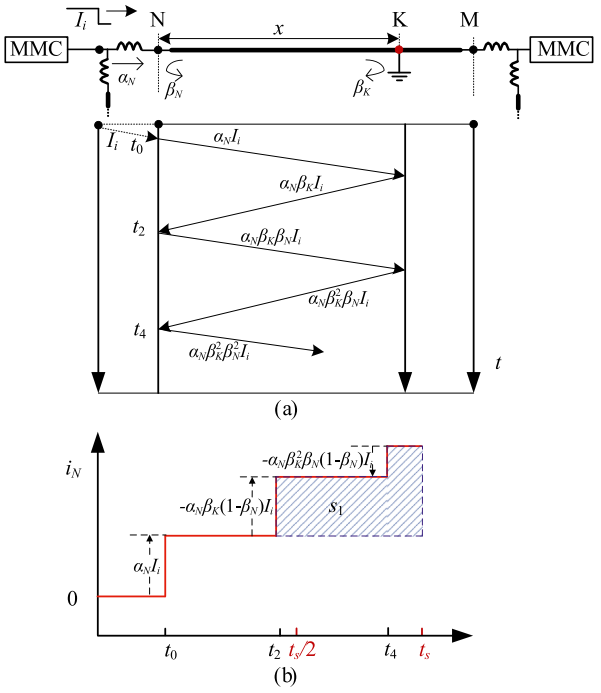

Fig. 9. Lattice diagram of injected TW and characteristics of i_N under internal metallic fault.

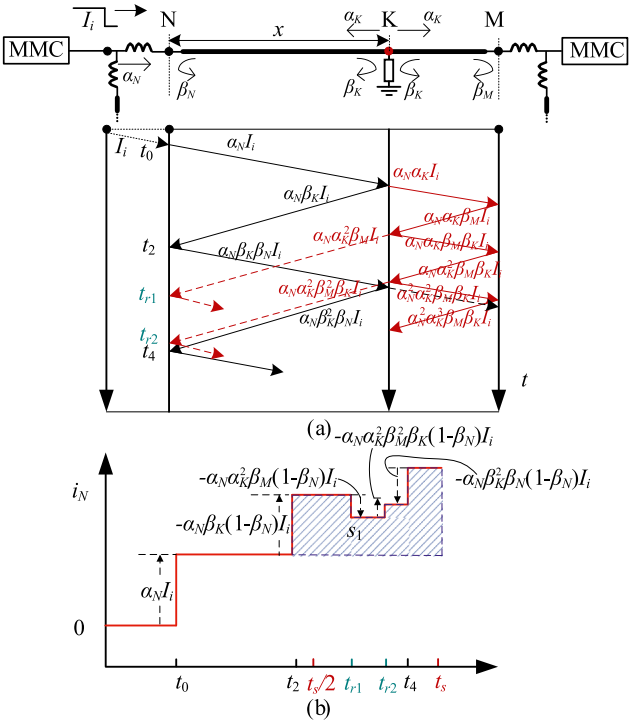

Fig. 10. Lattice diagram of injected TW and characteristics of i_N under internal fault with resistance.

(2) Metallic internal faults.

Under an internal metallic fault, the injected TW will only propagate between the terminal N and the fault point K, because the refraction coefficient α_K at the fault point is zero. The Lattice diagram of injected TW is shown in Fig. 9(a). Similarly, the injected current TW I_i refracts $\alpha_N I_i$ into the transmission line and causes the measured current i_N to rise

at t_0. Meanwhile, i_N rises again at t_2 by $-\alpha_N\beta_K(1-\beta_N)I_i$, where the reflection coefficient β_K is smaller than zero. At t_4, there is an increase by $-\alpha_N\beta_K^2\beta_N(1-\beta_N)I_i$ when the TW reflects back to the terminal N for the second time. According to the above analysis, the changing characteristics of measured current i_N within (t_0, t_s) are shown in Fig. 9(b). It demonstrates that the i_N within (t_2, t_s) is larger than the value of i_N at t_2. Therefore, the shaded current area s_1 enclosed by the value of current i_N at t_2 and the measured value of current i_N within (t_2, t_s) is positive.

(3) Internal faults with resistance.

Under an internal fault with resistance, the injected TW can refract into another section of the transmission line (from the fault point K to the terminal M), and the refraction coefficient α_K is greater than zero. The Lattice diagram of injected TW is shown in Fig. 10(a). Compared with the scenario of internal metallic fault, some reflected TWs from the terminal M like $\alpha_N\alpha_K^2\beta_M I_i$ and $\alpha_N\alpha_K^2\beta_M^2\beta_K I_i$ reach terminal N at t_{r1} and t_{r2}, respectively. The arrival of these TWs will also make the change in the measured terminal current i_N. However, the influence of these reflected TWs from terminal M is little, because the amplitudes after multiple refractions and reflections have been greatly reduced. As shown in Fig. 10(b), the shaded current area s_1 enclosed by the value of current i_N at t_2 and the measured value of current i_N within (t_2, t_s) is positive.

Based on the different propagation processes at the different discontinuity points, the characteristics of the injected TW will vary. Comparing the difference of the measured current i_N under the different faults, the shaded current area s_1 is negative and positive under the external and internal faults, respectively. Therefore, the polarity of the shaded current area can be used to identify the faults.

3. Control strategies of MMC

C. Fault ride-through process.

For the hybrid-MMC, FBSMs and HBSMs are both introduced into the bridge arm, and FBSMs are still controllable.

after a DC fault occurs. The converter topology is shown in Fig. 11. Based on the high controllability of hybrid-MMC, the negative voltage output characteristics of the FBSMs can be used to realize the DC fault ride-through.

Before the fault occurs, the control strategy of the hybrid-MMC is consistent with the traditional control strategy (mode 1) based on the HB-MMC, as shown in Fig. 12. After the detection of the fault, the control strategy switches to the fault ride-through mode (mode 2). The HBSMs in the bridge arm are bypassed, and FBSMs are used to output the negative voltage. By introducing DC current feedback control, the reference DC offset voltage $u_{dc/2}$ of the bridge arm can be controlled.

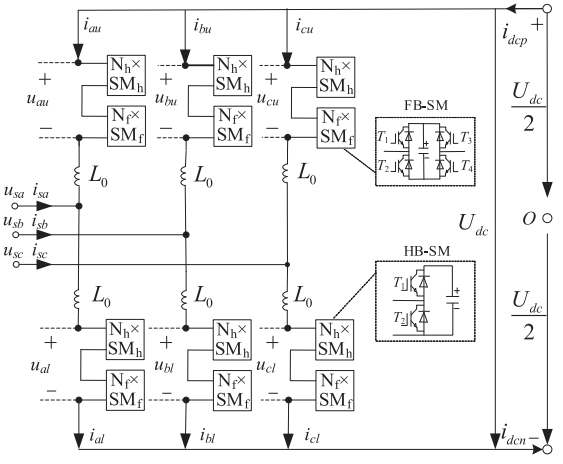

Fig. 11. Topology of hybrid MMC.

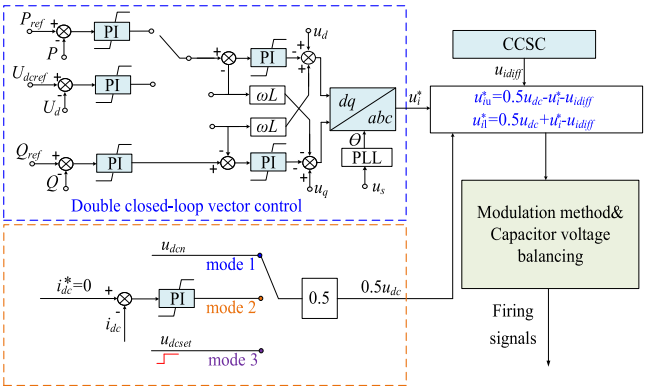

Fig. 12. Block diagram of MMC control strategies.

Therefore, a negative reference DC offset voltage of the bridge arm is generated by the difference between i_{dc} and the reference i_{dc}*. Finally, the DC fault current can be limited to zero quickly.

D. Active injection strategy.

After the fault ride-through process, the selected MMC will switch the control strategy to mode 3 and injects a rectangular TW into the transmission lines. As shown in Fig. 12, u_{dcset} is the designed output voltage of MMC. The characteristics of the injected TW are discussed below.

(1) Amplitude of injected TW.

The amplitude of the injected TW should consider two aspects. Firstly, the amplitude of the injected TW should not be too large, because the injected TW might cause the fluctuation of the system. Secondly, the changing characteristics of the measured terminal current should be notable under the injected TW.

After the fault ride-through process, there is no power transfer in the transmission lines. Therefore, the initial value of the measured terminal current is zero and the change in the measured terminal current is only caused by the injected TW. The small amplitude of the injected TW can theoretically ensure the detectability of the measured terminal current. However, the attenuation of the TW should also be considered. The TW contains signals of different frequencies, and the wavefront amplitude can be regarded as the sum of the wavefront amplitude of each frequency component.

$$A_h = \sum_i \mathrm{e}^{-\gamma(\omega_i)x} f_{\omega_i}(t) \tag{11}$$

where ω_i is the angular frequency corresponding to the different frequencies; A_h is the amplitude of the wave front; $f_{\omega i}(t)$ is the initial amplitude of the wavefront at different frequencies; x is the TW propagation distance; and $\gamma(\omega_i)$ is the attenuation coefficient.

The attenuation coefficient $\gamma(\omega_i)$ is:

$$\gamma(\omega_i) = \alpha(\omega_i) + j\beta(\omega_i) = \sqrt{[R(\omega_i) + j\omega_i L(\omega_i)][G(\omega_i) + j\omega_i C(\omega_i)]} \tag{12}$$

where $R(\omega_i)$, $L(\omega_i)$, $G(\omega_i)$, and $C(\omega_i)$ denote series resistance, series inductance, parallel conductance, and parallel capacitance per unit length, respectively. The real part of $\gamma(\omega_i)$ is the attenuation constant $\alpha(\omega_i)$, and the imaginary part represents the phase constant $\beta(\omega_i)$.

According to (11)-(12), as the propagation distance increases, the amplitude of each frequency component of the injected TW signal has different degrees of attenuation. As shown in Fig. 13, the higher the frequency component, the more severe the amplitude attenuation. The measured current is the time domain quantity of the whole frequency band. Even if the attenuation is severe in the high-frequency band, the attenuation in the low-frequency band is small. Therefore, the influence of the line attenuation within t_s can be approximately ignored. Based on the analysis above, u_{dcset} is set to be 0.1p.u.

(2) Length of injected TW.

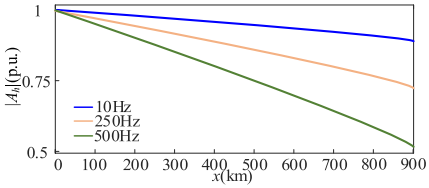

Fig. 13. Line-mode TW attenuation under different frequencies.

Based on the analysis of characteristics of the measured current in Section IV, the time to calculate the shaded current area is up to t_s, which contains the four times for the TW to propagate over the entire transmission line. t_s is determined by TW velocity, and the expression of the TW velocity is:

$$v(\omega_i) = \frac{\omega_i}{\beta(\omega_i)} \tag{13}$$

According to (13), different frequency components in TW have different propagation velocities. The high-frequency components of TW propagate faster than the low-frequency components. As shown in Fig. 14, the line-mode TW velocity has a nonlinear increasing relationship with the frequency. The injected TW contains frequency components from zero to infinity, and they will be affected under different propagation velocities. Therefore, the wavefront only contains high-frequency components, and the wave tail contains both high-frequency and low-frequency components. The low-frequency components dominantly affect the characteristics of the measured terminal current. Therefore, the wave velocity v is considered to be 292 km/ms. Since the longest transmission line in the grid is 200 km, t_s is calculated to be 2.740 ms. Meanwhile, when the control strategy switches back to mode 2, it will also cause a sudden change in the converter outlet voltage, affecting the characteristics of the measured terminal current. Therefore, the injection time should be slightly longer than t_s. The length of the injected TW is set to be 3 ms.

4. Overall scheme of active injection protection

E. Fault detection.

The low voltage and overcurrent criteria are used to detect the faults for the simple implementation, small amount of computation, and high speed.

$$u_{dc} < 0.7U_{dcn} || i_{dc} > 1.5I_{dcn} \tag{14}$$

where u_{dc} is the measured DC voltage; U_{dcn} is the rated DC voltage; i_{dc} is the measured DC current; I_{dcn} is the rated DC current. Once (14) is satisfied, the MMC will switch to the control mode 2 to limit the fault current.

F. Faulty pole discrimination.

The ratio of the transient voltages between the positive and negative poles is used to identify the faulted pole. The criterion is:

$$\frac{\sqrt{\int |u_{dc,P}|^2 dt}}{\sqrt{\int |u_{dc,N}|^2 dt}} = E_{ratio}, \begin{cases} E_{ratio} > E_{set}(positive\ pole\ fault) \\ E_{ratio} < 1/E_{set}(negative\ pole\ fault) \\ 1/E_{set} \le E_{ratio} \le E_{set}(pole\ -\ to\ -\ pole\ fault) \end{cases} \tag{15}$$

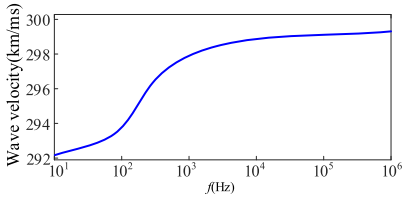

Fig. 14. Line-mode TW velocities under different frequencies.

where the subscripts P represents the positive pole and N represents the negative poles; and E_{ratio} is the ratio of transient voltage energy between the positive and negative poles. With the consideration of the discharge of distributed capacitance and noise disturbance, E_{ratio} is not equal to 1 strictly when the PTP fault occurs. Then, the reliability coefficient E_{set} is set to be 2. Under the positive pole-to-ground (P-PTG) fault and PTP, the converter in the positive pole will be selected to start the injection process. Under the negative pole-to-ground (N-PTG) fault, the selected converter is in the negative pole.

G. State detection of current.

Considering the influence of current fluctuation and the noise interference, the state of the fault current should be detected whether the fault currents are limited to zero. Therefore, the gradient grad(i) is proposed to detect the state of fault current.

$$|grad[i(k)]| = \sum_{j=0}^{4} i(k-j) - \sum_{j=5}^{9} i(k-j) < \Delta I_{set} \tag{16}$$

where $i(k\text{-}j)$ is the jth sampled current prior to the present moment; and ΔI_{set} is the threshold, which is set to be 0.03.

H. Fault identification.

Based on the analysis of the variation of the terminal measured current in Section IV, the shaded current area s_1 is negative and positive under the internal and external faults, respectively. These characteristics of the measured terminal current are used for the fault identification. Owing to the low amplitude of the injected TW and the short time window, the area of s_1 is not very large numerically. Therefore, the area index λ is proposed to evaluate the polarity of the measured current area.

$$\lambda = \sum_{k=t_s/(2\Delta t)+1}^{t_s/(\Delta t)} \frac{i_k - i_{t_s/2}}{t_k - t_{t_s/2}} > A_{set} \tag{17}$$

where t_s is the end time defined in Section IV; Δt is the sampling interval; $i_{t_s/2}$ is the measured terminal current at $t_{s/2}$; k is the sequence number; and A_{set} is the threshold, which is set to be 0.

As analyzed in Section IV, the time of the first return of the TW is t_2, which is related to the position of the fault point. Although t_2 is an indeterminate quantity, the start time t_0 and the end time t_s of the TW injection are fixed. Therefore, the data within $[t_s/2, t_s]$ is used for the fault identification. Under the external fault, area index λ must be significantly negative. Under the internal fault, area index λ must be the positive. Fault resistance has some influence, but does not change the polarity of the area index.

I Active injection strategy.

The converters will be activated in sequence to inject the TW, avoiding the disturbance of the TW from the adjacent converter. Therefore, the sequence of converters to start active injection control is designed in advance: $MMC_1 \rightarrow MMC_2 \rightarrow MMC_3$. The detailed injection starting criterion of each converter is shown in Fig. 15. Once MMC_1 detects that the fault current of the system has been suppressed to zero, it will start to inject a characteristic TW into the transmission line. Meanwhile, MMC_2 and MMC_3 will also detect the change in the current caused by the TW from MMC_1. Therefore, when the MMC_2 detects twice that the fault current has been suppressed to zero, MMC_2 will be activated to inject the characteristic TW. Similarly, after recognising that the fault current has been suppressed to zero for three times, MMC_3 will start to inject the characteristic TW.

J. Overall scheme of proposed protection.

Based on the criteria above, the process of the entire protection scheme is shown in Fig. 16. After the detection of the fault, all the converters in the grid will switch to control mode 2 to limit the fault currents to zero. At the same time, the fault pole can also be discriminated by the calculated ratio of the transient voltages. The research objective is a three-terminal HVDC grid, as shown in Fig. 1. Converters will inject the rectangular TWs to identify the fault in the order of MMC_1,

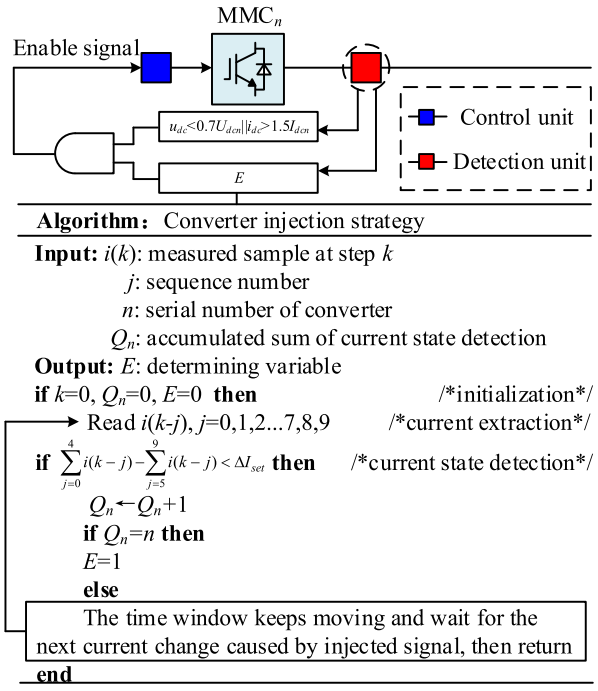

Fig. 15. Active injection strategy of converters.

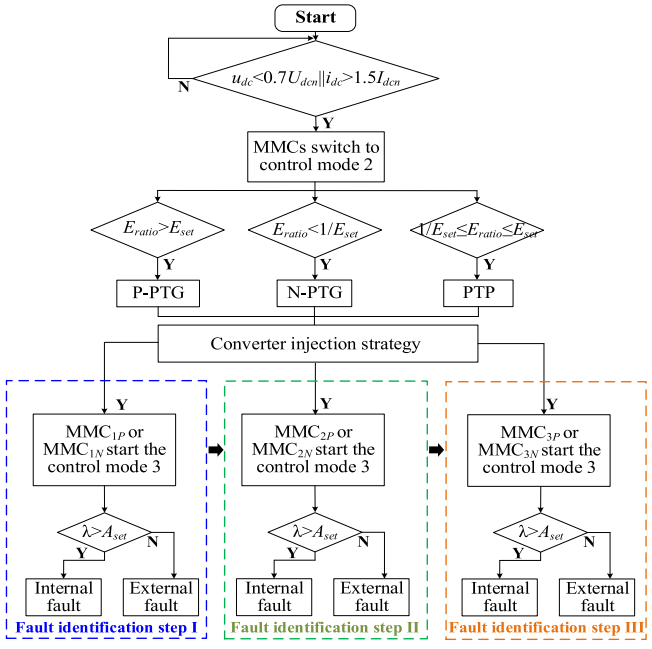

Fig. 16. Flowchart of proposed protection.

MMC$_2$, and MMC$_3$. After the fault current is suppressed to zero, MMC$_1$ will switch to control mode 3 to inject a rectangular TW to identify whether the two lines connected to MMC$_1$ are faulty. The injected TW will also cause the current change measured by MMC$_2$. After the state detection of the current, MMC$_2$ will start to inject a rectangular TW to identify the fault. Similarly, MMC$_3$ will also carry out the same fault identification process. Finally, the fast disconnecting switches on both sides of the line will isolate the fault.

5. Simulation validation

To verify the performance of the proposed protection scheme, a ± 500 kV three-terminal bipolar hybrid MMC-HVDC grid depicted in Fig. 17 is constructed by PSCAD/EMTDC. The grid consists of three transmission lines L_{12}(200 km), L_{13}(200 km), and L_{23}(200 km), which adopt the frequency-dependent model. Meanwhile, further details of the simulation system along with its parameters are listed in Table 1. The sampling frequency is 10 kHz in the simulation.

K. Verification of fault identification.

f_1, f_2, and f_3 are the metallic P-PTG faults occurring in the middle of L_{12}, L_{23}, and L_{13}, respectively. The fault occurs at t = 1 s. Taking the protection unit N as an example to verify the performance of the proposed protection, the simulation results are shown in Figs. 18-20. Furthermore, the output voltage of the MMC$_1$ is shown in Fig. 18(a)-20(a). The measured current i_N is shown in Fig. 18(b)-20(b). TW$_{(1)}$, TW$_{(2)}$, and TW$_{(3)}$ represents the changes of voltage and current caused by the TW injected by MMC$_1$, MMC$_2$, and MMC$_3$, respectively. Meanwhile, the detailed information of i_N during the TW injection process is shown in Fig. 18(c)-20(c).

1) Internal fault f_1.

The fault can be detected quickly, and the converters will step into the fault ride-through process. After the fault currents are limited to zero, MMC$_1$ injects a rectangular TW into the transmission line firstly, as shown in Fig. 18. Correspondingly, the measured current i_N will also change with the reflection and refraction of the injected TW. During the injection process, i_N will keep increasing. The shaded current area s_1 enclosed by the value of current i_N at t_s/2 and the measured value of current i_N within (t_s/2, t_s) is positive. The calculated area index λ is 2421, satisfying (17). Therefore, an internal fault in L_{12} can be identified by the proposed protection scheme.

2) External faults f_2 and f_3.

For the forward external fault f_2 and the backward external f_3, the characteristics of the measured current i_N within the injection process are different compared with the characteristics under the internal fault. As shown in Fig. 19(c)-20(c), i_N decreases from t_s/2, and the shaded current area s_1 enclosed by the value of current i_N at t_s/2, and the measured value of current i_N within (t_s/2, t_s) is negative. The calculated area index λ are −614 and −489 under f_2 and f_3, respectively. Therefore, the external faults will not cause the misoperation of the proposed protection.

L. Influence of fault resistance.

To verify the robustness of the proposed protection scheme against fault resistance. The P-PTG faults with different resistances varying from 0.1 Ω to 1000 Ω are set to occur at different locations. Here, 0%-100% is defined that the fault location in line L_{12} varies from terminal N to terminal M. The calculated results of the area index λ are listed in Table 2. It can be seen that the most severe situation is under $f_{1(100\%)}$ with 1000 Ω, and the measured current i_N during the injection process is shown in

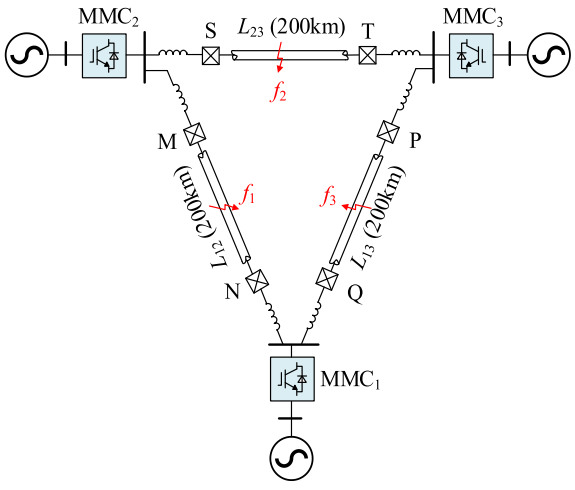

Fig. 17. Simulation system of three-terminal hybrid-MMC HVDC grid.

Table 1
Major parameters of the simulation system.

Parameters	Converters		
	MMC_1	MMC_2	MMC_3
Power capacity/MW	500	500	1000
Number of SMs per arm	200	200	200
SM capacitance/mF	10	10	15
Arm inductance/mH	75	75	75
CLR/mH	100	100	100

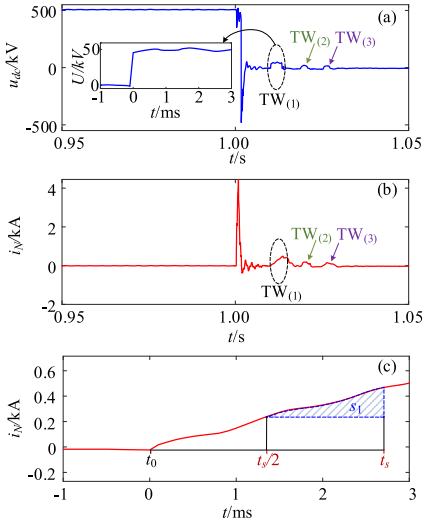

Fig. 18. Fault characteristics under f_1.

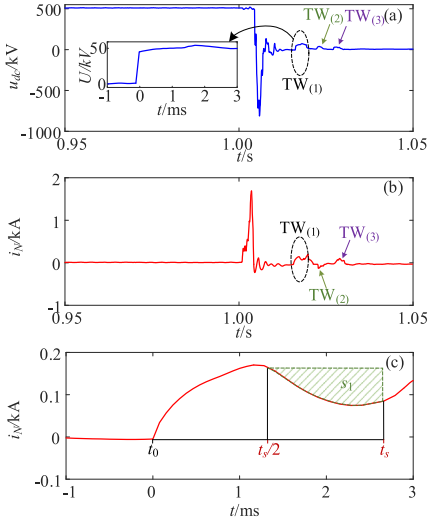

Fig. 19. Fault characteristics under f_2.

Fig. 21. The area index λ reaches a small value (1 1 8). However, the fault can be still identified reliably. Moreover, the external faults will not cause the misoperation of the proposed protection scheme with 1000 Ω fault resistance.

M. Influence of CLR.

To verify the influence of the size of CLR, different sizes of CLR are set to test the performance of the proposed protection scheme. The simulation results are listed in Table 3 under the CLR from 20 mH to 200 mH, and the measured current i_N under the internal fault $f_{1(50\%)}$ and external fault $f_{2(50\%)}$ is also demonstrated in Fig. 22. It can be seen that

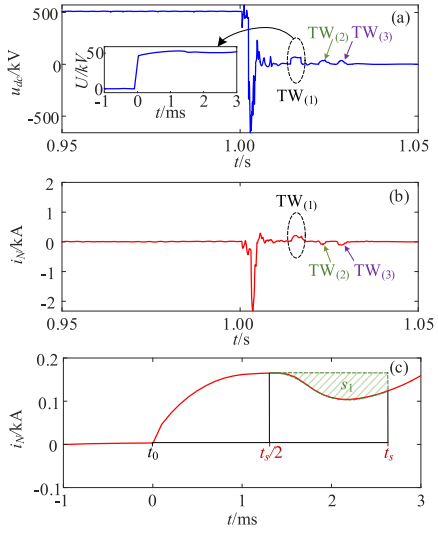

Fig. 20. Fault characteristics under f_3.

Table 2
Simulation results under different fault resistances.

Faults	Fault resistance/Ω	Area index λ	Fault identification
$f_{1(0\%)}$	0.01	5412	Internal fault
	1000	398	Internal fault
$f_{1(50\%)}$	0.01	2421	Internal fault
	1000	274	Internal fault
$f_{1(100\%)}$	0.01	1650	Internal fault
	1000	118	Internal fault
$f_{2(50\%)}$	0.01	−1284	External fault
	1000	−614	External fault
$f_{3(50\%)}$	0.01	−1032	External fault
	1000	−489	External fault

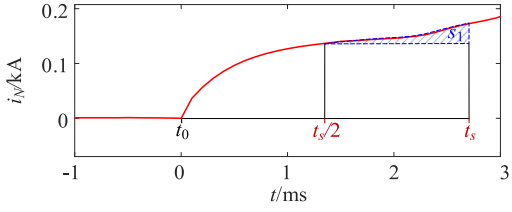

Fig. 21. Measured current i_N under $f_{2(100\%)}$ with 1000 Ω resistance.

Table 3
Simulation results under different CLRs.

Faults	CLR/mH	Area index λ	Fault identification
$f_{1(50\%)}$	20	3214	Internal fault
	100	2421	Internal fault
	200	1856	Internal fault
$f_{2(50\%)}$	20	−445	External fault
	100	−1284	External fault
	200	−1875	External fault
$f_{3(50\%)}$	20	−417	External fault
	100	−1032	External fault
	200	−1810	External fault

the areas of $S_{I(20mH)}$, $S_{II(100mH)}$, and $S_{III(200mH)}$ are in a decreasing trend under the internal fault and in an increasing trend under the external fault. The proposed protection can still identify the fault under different values of CLR.

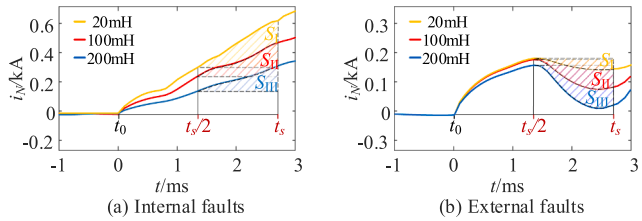

Fig. 22. Measured current i_N under Internal and external faults under different CLRs.

N. Influence of noise interference.

The 30 dB white noise is superimposed on the measured current i_N under different metallic P-PTG faults to test the noise enduring capability of the proposed protection scheme. The simulation results are listed in Table 4, which indicates that the 30 dB white noise will not influence the performance of fault identification.

O. Influence of line length.

As analyzed in Section III.B, the reflection characteristics at the terminals N (active injection mode) and M (fault ride-through mode) are different. For a 200 km transmission line, the protection time window is $t_s = 4\ l/v < 3$ ms (The TW travels on the line for four full lengths of time). Therefore, it can be considered that the reflection coefficients β_N and β_M are within (-1, 0) and (0, 1) respectively. However, if the line length is too long and causes that $t_s > 4.4$ ms, the change of β_M will influence the reliability of the proposed protection method theoretically. Based on the simulation system in Fig. 17, the line length is set to 400 km and an external fault f_2 is set to verify the protection unit N. As shown in Fig. 23, the calculated area index λ is −21. It can be seen that the variation trend of i_N is changed because of the change of β_M. The positive area s_2 occurs and affects the fault identification, causing the risk of protection misoperation. However, in real projects, the maximum line length of VSC-HVDC grids is about 200 km [26]. Therefore, the proposed protection satisfies the requirement of practical projects.

P. Operation time of protection.

The fault currents are dominated by the discharging capacitors in the circuit. Due to the fault current limiting capacity of the hybrid-MMC, the fault currents can be limited effectively. The fault ride-through process can be completed within 10 ms based on the simulation results [25]. The injection process of each converter is 3 ms. Due to the amplitude of the injected TW being small, the fluctuation caused by the injected TW can also be suppressed quickly. The interval between the start of the injection process of converters is smaller than 3 ms based on the simulation. Therefore, the total operation time of the proposed protection will not exceed 30 ms after the fault occurs.

6. Conclusion

In this paper, a new active injection protection scheme has been proposed for the multi-terminal HVDC grid, with the integration of the high controllability of the hybrid-MMC. The fault can be identified with high reliability and sensitivity, without any additional injection equipment. The simulation results illustrate that the proposed scheme has the excellent capability of enduring the fault resistance and noise interference. Compared with the existing active injection based protection schemes, the injected signal of the proposed scheme is simpler, and the protection algorithm is computationally light. Furthermore, this protection scheme has a low dependency on the size of CLR, thus presenting a promising solution for future multi-terminal HVDC grid protection.

Dear Editor and Reviewers,

We would like to thank the International Journal of Electrical Power and Energy Systems for allowing us to revise our manuscript.

Many thanks for the insightful comments and suggestions of the editor and reviewers. We believe that the additional changes we have made in response to the comments have made this a significantly stronger manuscript.

Table 4
Simulation results with noise disturbance.

Faults	Noise/dB	Area index λ	Fault identification
$f_{1(0\%)}$	30	5374	Internal fault
$f_{1(50\%)}$	30	2466	Internal fault
$f_{1(100\%)}$	30	1593	Internal fault
$f_{2(50\%)}$	30	−1342	External fault
$f_{3(50\%)}$	30	−1019	External fault

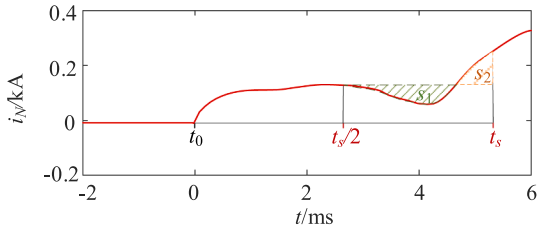

Fig. 23. Measured current i_N under f_2 when line length is 400 km.

We have modified the manuscript accordingly and carefully. The texts in **RED** are the changes we have made in the revised manuscript. Detailed corrections and responses to the comments are listed below point to point.

Thanks very much for your consideration of our paper.

Yours faithfully.

Authors.

This work is supported by National Natural Science Foundation of China-State Grid Joint Fund for Smart Grid (No. U2066210). National Natural Science Foundation of China (NSFC) (No. 52007003).

Declaration of Competing Interest

The authors declare that they have no known competing financial interests or personal relationships that could have appeared to influence the work reported in this paper.

Data availability

The authors do not have permission to share data.

References

[1] Meyer C, Hoing M, Peterson A, De Doncker RW. Control and Design of DC Grids for Offshore Wind Farms. IEEE Trans Ind Appl Nov. 2007;43(6):1475–82.
[2] Li Y, Tang G, Ge J, He Z. Modeling and damping control of modular multilevel converter based DC grid. IEEE Trans Power Syst Jan. 2018;33(1):723–35.
[3] Adeuyi OD, Cheah-Mane M, Liang J, Jenkins N. Fast frequency response from offshore multi-terminal VSC-HVDC schemes. IEEE Trans Power Delivery Dec. 2017; 32(6):2442–52.
[4] Elserougi AA, Abdel-Khalik AS, Massoud AM, Ahmed S. A new protection scheme for HVDC converters against DC-side faults with current suppression capability. IEEE Trans Power Delivery Aug. 2014;29(4):1569–77.
[5] Sneath J, Rajapakse AD. Fault detection and interruption in an earthed HVDC grid using ROCOV and hybrid DC breakers. IEEE Trans Power Del Jun 2016;31(3): 973–81.
[6] M. Callavik, A. Blomberg, J. Hafner, and B. Jacobson, "The hybrid HVDC breaker: An innovation breakthrough enabling reliable HVDC grids," ABB Grid Syst., Tech. Paper, Nov. 2012.
[7] Bucher MK, Franck CM. Contribution of fault current sources in multiterminal HVDC cable networks. *IEEE Trans Power De*l May 2013;28(3):1796–803.
[8] X. Li, B. Zhao, Y.Wei, X. Xie, Y. Hu, and D. Shu. "DC fault current limiting effect of MMC submodule capacitors," *Int. J. Electr. Power Energy Syst.*, vol. 115, Feb. 2020, Art. no. 105444.
[9] Wang S, Li C, Adeuyi OD, Li G, Ugalde-Loo CE, Liang J. Coordination of MMCs with hybrid DC circuit breakers for HVDC grid protection. IEEE Trans Power Del Feb. 2019;34(1):11–22.
[10] Cui S, Sul S. A comprehensive dc short-circuit fault ride through strategy of hybrid modular multilevel converters (MMCs) for overhead line transmission. IEEE Trans Power Electron Nov. 2016;31(11):7780–96.

[11] Jovcic D, Lin W, Nguefeu S, Saad H. Low-energy protection system for DC grids based on full-bridge MMC converters. IEEE Trans Power Del Aug. 2018;33(4):1934–43.
[12] Lin W, Jovcic D, Nguefeu S, Saad H. Full bridge MMC converter optimal design to HVDC operational requirements. IEEE Trans Power Del Jun. 2016;31(1):1342–50.
[13] He J, Chen K, Li M, et al. "Review of protection and fault handling for a flexible DC grid", *Protection and Control of*. Modern Power Systems May. 2020.;5(15):1–15.
[14] Kong F, Hao Z, Zhang S, Zhang B. Development of a novel protection device for bipolar HVDC transmission lines. IEEE Trans Power Delivery Oct. 2014;29(5):2270–8.
[15] Sneath J, Rajapakse AD. Fault detection and interruption in an earthed HVDC grid using ROCOV and hybrid DC breakers. IEEE Trans Power Delivery June. 2016.;31(3):973–81.
[16] Liu J, Tai N, Fan C. Transient-Voltage-Based Protection Scheme for DC Line Faults in the Multiterminal VSC-HVDC System. IEEE Trans Power Delivery June 2017;32(3):1483–94.
[17] Zhang C, Li Y, Song G, Dong X. Fast and Sensitive Nonunit Protection Method for HVDC Grids Using Levenberg–Marquardt Algorithm. IEEE Trans Ind Electron Sept. 2022;69(9):9064–74.
[18] Farshad M. A Pilot Protection Scheme for Transmission Lines of Half-Bridge MMC-HVDC Grids Using Cosine Distance Criterion. IEEE Trans Power Delivery Apr. 2021;36(2):1089–96.
[19] Qing H, et al. A pilot line protection for MT-HVDC grids using similarity of traveling waveforms. Int J Electr Power Energy Syst Oct. 2021;131:107162.
[20] Jia K, Shi Z, Wang C, Li J, Bi T. Active Converter Injection-Based Protection for a Photovoltaic DC Distribution System. IEEE Trans Ind Electron June 2022;69(6):5911–21.
[21] Zhu R, et al. Active control-based protection for a flexible DC system of a PV power plant. Int J Elect Power Energy Syst Feb. 2020;114:105413.
[22] Wang T, Song G, Hussain KST. Adaptive Single-Pole Auto-Reclosing Scheme for Hybrid MMC-HVDC Systems. IEEE Trans Power Del Dec. 2019;34(6):2194–203.
[23] Hou J, Song G, et al. Single-end fault identification scheme for multi-terminal DC grid based on amplitude similarity of injection signal. Int J Elect Power Energy Syst Oct. 2021;131:107091.
[24] Li M, et al. "Full-current-based directional pilot protection for VSC-DC distribution systems", *IET Gen*. Transm Distrib June. 2019.;13(16):3713–24.
[25] Wenig S, Goertz M, Hirsching C, Suriyah M, Leibfried T. On Full-Bridge Bipolar MMC-HVDC Control and Protection for Transient Fault and Interaction Studies. IEEE Trans Power Del Dec. 2018;33(6):2864–73.
[26] High-Voltage Direct Current (HVDC) Power Transmission Using Voltage Sourced Converters (VSC), IEC/TR 62543, 2011.